Article

Not peer-reviewed version

Pvdf-Based Polymer Composites Filled with Ti3C2Tx MXene / Magnetic Nanoparticle Heterostructures for Aquatic Dye Removal

Nikolay R. Shilov , Sayara E. Aga-Tagieva , Viktor M. Rybalchenko , Alexander Omelyanchik , Kirill V. Sobolev * , Rinat R. Aysin , Valeria V. Rodionova , Kurban E. Magomedov *

Posted Date: 19 November 2024

doi: 10.20944/preprints202411.1343.v1

Keywords: MXenes; PVDF; polymer composites; magnetic nanoparticles; Ti3C2Tx; CoFe2O4; Fe3O4; composite materials; dye removal; photocatalysis; sonocatalysis

 doi:10.20944/preprints202411.1343.v1

Article

PVDF-Based Polymer Composites Filled with $Ti_3C_2T_x$ MXene / Magnetic Nanoparticle Heterostructures for Aquatic Dye Removal

Nikolay R. Shilov [1], Sayara E. Aga-Tagieva [2], Viktor M. Rybalchenko [1], Alexander S. Omelyanchik [1], Kirill V. Sobolev [3,*], Rinat R. Aysin [4], Valeria V. Rodionova [1], and Kurban E. Magomedov [1,*]

1 REC Smart Materials and Biomedical Applications, Immanuel Kant Baltic Federal University,A. Nevskogo Str. 14, 236014 Kaliningrad, Russia
2 SCAMT Laboratory, ITMO University, Lomonosova Str. 9, 191002, St. Petersburg, Russia
3 Department of Materials Engineering, Ben Gurion University of the Negev, P.O. Box 653, Beer-Sheva 8410501, Israel
4 A. N. Nesmeyanov Institute of Organoelement compounds, Russian Academy of Sciences, ul. Vavilova 28, str. 1, Moscow, 119334 Russia
* Correspondence: kirill.sobolev.off@gmail.com (K.V.S.); m_kurban@mail.ru (K.E.M.)

Abstract: This study presents the development and characterization of novel polyvinylidene fluoride (PVDF)-based polymer composites for environmental remediation applications. We synthesized composites incorporating three types of fillers: $Ti_3C_2T_x$ MXenes, magnetic nanoparticles ($CoFe_2O_4$ and γ-Fe_2O_3/Fe_3O_4), and their heterostructured combinations. To enhance the homogeneity of the composites, the filler particles were additionally coated with polyethylene glycol (PEG). Photocatalytic and sonocatalytic degradation of methylene blue (MB) dye was evaluated under light and ultrasonic irradiation, respectively. Experimental results demonstrated that PVDF-based nanocomposite with MXene/γ-Fe_2O_3/Fe_3O_4 heterostructures as the filler achieves a significant MB photocatalytic degradation rate of 40.3% within 60 minutes. Simultaneously, MXene/$CoFe_2O_4$-containing nanocomposite exhibits outstanding performance in sonocatalysis, achieving a reduction in MB concentration exceeding 45% over a similar treatment duration. These findings highlight the potential of PVDF-MXene-MNPs composite materials in environmental remediation technologies, emphasizing the critical role of PVDF as a primary component and a suitable host matrix in catalytic processes.

Keywords: MXenes; PVDF; polymer composites; magnetic nanoparticles; $Ti_3C_2T_x$; $CoFe_2O_4$; Fe_3O_4; composite materials; dye removal; photocatalysis; sonocatalysis

1. Introduction

The textile industry is one of the largest sources producing tons of waste dyes, which, even at low concentrations, reduce wastewater transparency and oxygen solubility, and are toxic [1–3]. Dyeing and finishing processes are among the main causes of textile wastewater generation. These processes use a large number of different inputs such as chemicals and dyes, and unfortunately, not all the inputs are fully contained in the final product; therefore, they become waste and are discharged into the environment [4,5]. The main reason for obstacles in textile wastewater treatment is the difficulty in dealing with the chemical structure of textile chemicals [6]. Contaminants exist in the form of suspended solids, color, acidity, and chemical oxygen demand [7]. In addition, pH can vary over the wide range from 2 to 12, which complicates the task of selecting proper treatments [8,9].

Photocatalysis, which breaks down dye molecules, can be used to treat wastewater from this type of pollutants [10–14]. In addition to the photocatalytic effect, piezoelectric effect can be used to improve water purification [15–20]. The piezoelectric effect enhances photocatalysis through stress-induced generation of an internal electric field, which promotes the separation and migration of photogenerated electron-hole pairs, thereby providing higher piezophotocatalytic efficiency. Compared to relatively mature research in photocatalysis, piezocatalysis is considered as a new strategy to combat environmental pollution and energy scarcity [21]. Currently, research on the application

 doi:10.20944/preprints202411.1343.v1

of piezocatalytic systems is still under development. However, it is already clear that widespread practical application of heterogeneous standby photo-, piezo-, and piezophotocatalysts is difficult due to their non-uniform distribution and the difficulty of catalyst extraction and reuse. Immobilization of the catalyst on a polymer matrix may be a solution to these problems [22–24].

During the sonochemical process, ultrasonic waves cause rapid growth and cavitation collapse of bubbles in the solution, resulting in extremely high temperature and pressure in the bubble. Consequently, the high temperature in the vicinity of the bubbles leads to thermal dissociation of water, resulting in the formation of hydroxyl radicals (OH^-) as one of the most powerful oxidants for non-selective oxidation of target organic pollutants[25,26]. However, complete mineralisation of target pollutants by sonolysis alone requires a large amount of energy and long reaction times. To solve this problem, ultrasonic irradiation in the presence of an appropriate semiconductor as a sonocatalyst can be performed to accelerate the reaction [27]. Among these techniques, piezocatalysis has made significant progress in environmental remediation due to the ability to convert mechanical energy into chemical energy by harvesting it from various motions (wind, noise, water flow, etc.) [28,29]. It is widely accepted that piezocatalysis is associated with piezoelectric polarization caused by the deformation of non-centrosymmetric materials during mechanical energy capture [30,31]. In principle, strain-induced polarization leads to a deflection of the center of positive and negative charges within the unit cell, then a piezoelectric potential is generated, which drives free charge carriers towards opposite surfaces, where they can participate in redox reactions [32,33]. Hence, it is crucial to develop efficient piezocatalytic materials that can be effectively applied to purify contaminated water. In recent years, polymer composites based on PVDF and semiconductor nanoparticles, the so-called heterophase doping, were intensively studied for the purposes of piezocatalysis and piezophotocatalysis [34].

MXenes are a new class of two-dimensional materials with the general formula $M_{n+1}X_nT_x$, where M is a transition metal, X is carbon and/or nitrogen, T_x is a functional group, and n is an integer index typically varying from 1 to 4 [35]. Despite their relatively recent appearance, MXenes have already attracted the attention of scientists worldwide due to their unique properties: hydrophilicity, metallic conductivity, large specific surface area, etc.. Moreover, due to the active surface of MXenes, they can be functionalized, which makes it possible to tune their properties as well as to induce the new ones [36,37]. All this allowed finding a large number of possible applications, for example, in biomedicine, energy harvesting, ecology, sensors, catalysis etc. [38].

One promising application of MXenes is the aquatic adsorption of toxic pollutants, such as heavy metal and radioactive ions, pharmaceuticals and dyes [39–42]. Among the dyes released into the environment and water resources, methylene blue (MB) is widely used in the textile industry. This dye is released into the environment during incomplete washing of products and can pose a serious hazard to humans and animals. Therefore, an effective method for complete and efficient decomposition of this pollutant in aqueous samples is required [43–49]. As addressed above, one of the most promising approaches to decomposing industrial wastes in the environmental water is an advanced oxidation process. This organic waste disposal technology is based on the creation of non-selective and oxidizing species capable of oxidizing various organic pollutants [50,51].

Magnetic nanoparticles (MNPs) represent another class of materials that are increasingly utilized in photocatalysis [52,53]. Their unique properties enable enhanced efficiency in degrading organic pollutants and improving the overall effectiveness of photocatalytic processes. MNPs facilitate enhanced separation and recovery from reaction mixtures using an external magnetic field, addressing the common challenge of recovering photocatalysts from wastewater. This feature significantly reduces secondary pollution and recovery costs associated with conventional photocatalysts [54].

The piezoelectric effect is used to enhance photocatalysis by an internal electric field, which promotes the separation and migration of photogenerated electron-hole pairs, thereby realizing higher piezophotocatalytic efficiency for the simultaneous use of these two types of natural energy. Combining photo- and piezocatalysis within a single material enables the utilization of two distinct energy sources—light and mechanical energy—to achieve enhanced efficiency in the decomposition of

 doi:10.20944/preprints202411.1343.v1

pollutants. This synergistic interaction not only enhances catalytic activity but also reduces recovery costs and minimizes secondary pollution, representing a significant advantage over conventional photocatalysts.

In this work, multilayer $Ti_3C_2T_x$ MXenes, and then MXenes functionalized with $CoFe_2O_4$ (CFO) and γ-Fe_2O_3/Fe_3O_4 (IO) [37] magnetic nanoparticles (MNPs) were synthesized, and all samples were coated with polyethylene glycol (PEG). All particles were then embedded into dissolved PVDF with dimethylformamide. After that, PVDF composite films with different fillers were obtained using doctor blade technique [55]. Finally, photocatalytic and sonocatalytic experiments were carried out with these polymer composites. MNPs enhanced the photocatalytic effect, and MXenes enhanced both the photocatalytic effect and the piezoelectric effect of PVDF polymer film. In addition to enhanced catalytic performance [56], the MNPs promote easy removal of the polymer composite from the aqueous medium after cleaning.

2. Materials and Methods

2.1. Materials

Lithium fluoride (LiF, Sigma-Aldrich, USA) and hydrochloric acid (HCl, Sigma Tech, Russia) were used to synthesize MXenes. Ferrous sulfate ($FeSO_4 \cdot 7H_2O$, LenReactiv, Russia), ferric chloride ($FeCl_3 \cdot 6H_2O$, Sigma-Aldrich, USA), cobalt nitrate ($Co(NO_3)_2 \cdot 6H_2O$, LenReactiv, Russia), sodium hydroxide (NaOH, Vekton, Russia) and aqueous ammonia 30% (NH_4OH, Sigma Tech, Russia) were used for the synthesis of MNPs. Polyethylene glycol (PEG, m.w. 3000, Sigma-Aldrich, USA) was used for the surface coating of MXenes, MNPs and MXene / MNPs heterostructures. Polyvinylidene fluoride (PVDF, Sigma-Aldrich, USA) and N,N-dimethylformamide (DMF, EKOS-1, Russia) were used to create functional polymer composites.

2.2. Synthesis of MXenes

Ti_3AlC_2 MAX phase precursor used for the synthesis of $Ti_3C_2T_x$ MXenes was produced and characterized as explained in works [57,58]. MXenes were obtained by selectively etching Al from the Ti_3AlC_2 precursor via the commonly used mild protocol [59]. 1 g of Ti_3AlC_2 (with particle size < 45 μm) was dissolved into 10 mL of 9M HCl in DDW water with 1.6 g of LiF, the reaction was maintained for 24 h at 35°C under constant magnetic stirring. After that, MXenes were centrifuged 7 times at 3000 rpm for 5 min with the addition of DDW water until reaching pH of about 6, then the solution was placed into an ultrasonic bath with ice for 30 min to provide additional delamination. Extra centrifugation cycle was then performed to separate multilayer MXenes and unreacted MAX phase leftovers from the single-layer $Ti_3C_2T_x$ MXene colloid suspension. The suspension was transferred and dried for the further studies, while the precipitate was dried separately at 45°C in a Petri dish overnight. This precipitate was further used for the synthesis of $Ti_3C_2T_x/Fe_3O_4$ and $Ti_3C_2T_x$/CFO heterostructures.

2.3. Synthesis of Magnetic Nanoparticles and MXene/MNPs Heterostructures

Fe_3O_4 iron oxide nanoparticles were obtained via ultrasound-assisted co-precipitation, as explained in more detail elsewhere [60]. Briefly, 0.25 mmol of ferrous sulfate and 0.5 mmol ferric chloride were dissolved into 5 ml of DDW, the solution was degassed in an ultrasound bath. Then the temperature of the ultrasonic bath was raised up to 80°C and an aqueous ammonia was added to achieve highly alkaline environment (pH > 11). After 1 h, the black precipitate was collected with a strong and subsequently was then dried in an oven at 80°C overnight.

Similarly, $CoFe_2O_4$ nanoparticles were synthesized using 0.6 mmol ferric nitrate and 0.3 mmol cobalt nitrate.

$Ti_3C_2T_x$ MXenes functionalized with Fe_3O_4 nanoparticles were produced as described in our previous work [37]. Briefly, the same ultrasound-assisted co-precipitation procedure was performed in presence of 50 mg of multilayer $Ti_3C_2T_x$ MXenes (i.e. precipitate from mild MXene synthesis) added before introducing ammonia solution. The remaining steps were identical to what was described

 doi:10.20944/preprints202411.1343.v1

previously for Fe_3O_4 synthesis, despite the drying temperature being reduced to 45°C to avoid the undesired oxidation of MXenes. The same procedure was utilized to produce $CoFe_2O_4$-based composites, but with 35 mg of MXenes dissolved initially in the solution with ferric and cobalt salts.

2.4. PEG-Coating of MXenes and Nanoparticles

To modify the surface of nanoparticles and MXene-based magnetic composites with PEG, 1 g of PEG was added into 10 ml of distilled water and homogenized in an ultrasonic bath for 30 min. Then, PEG was added to the nanoparticle suspension and dispersed for 3 h at 80°C. The supernatant was removed by centrifugation for 15 min at 3000 rpm, and the solid product was washed with water to remove unreacted PEG via magnetic separation. The final product was dried at 60°C for several hours.

2.5. Synthesis of Polymer-Based Nanocomposites

Piezoelectric PVDF was used as the host polymer matrix for the composite materials. PVDF granules were dissolved into DMF solvent at 40°C in a mass ratio of 1 : 8. To aid in dispersion, 20% of DMF total volume was separately used for the dispersion of $Ti_3C_2T_x$, nanoparticles, and MXene/MNPs heterostructures, keeping 10 wt.% of filler in all the polymer composite samples. Both the PVDF dissolution and the dispersion of nanoparticles and heterostructures were maintained under continuous stirring for 1 h. The dispersed particles were then added into the dissolved polymer, and further stirred for 30 min to ensure homogeneity.

Polymer-based nanocomposites were obtained via the solvent evaporation supported by the doctor blade technique to form thin films [55]. The polymers were applied onto pre-cleaned glass substrates, equalized using a coating spatula at a fixed spacing between the substrates. Then the substrates were placed into an oven to dry at 65°C overnight.

The summarizing description and labeling of all the such-obtained polymer-based nanocomposite samples is given in Table 1.

Table 1. List of the prepared and studied PVDF-based nanocomposites.

	Sample (group/ID)	Filler (10 wt.%)	PEG Coated
Pure Polymer	PVDF	-	-
MXene-based	MX-C	$Ti_3C_2T_x$	-
	MX@PEG-C	$Ti_3C_2T_x$	✓
Iron Oxide-based	IO-C	Fe_3O_4	-
	IO@PEG-C	Fe_3O_4	✓
	IO/MX-C	$Ti_3C_2T_x/Fe_3O_4$	-
	IO/MX@PEG-C	$Ti_3C_2T_x/Fe_3O_4$	✓
Cobalt Ferrite-based	CFO-C	$CoFe_2O_4$	-
	CFO@PEG-C	$CoFe_2O_4$	✓
	CFO/MX-C	$Ti_3C_2T_x/CoFe_2O_4$	-
	CFO/MX@PEG-C	$Ti_3C_2T_x/CoFe_2O_4$	✓

Note: A checkmark (✓) indicates PEG coating.

2.6. Structural and Chemical Characterization

X-ray diffraction (XRD) patterns were collected at room temperature by AXRD Benchtop (Proto Mfg., USA) powder X-ray diffractometer with 30 kV and 30 mA monochromatic Cu-Kα radiation with a step size of 0.015° and a counting time of 5 s per step at 2θ range of 5–80° to check the successful functionalization of MXenes with magnetic nanoparticles, crystallinity of MNPs and delamination of MXenes.

FTIR-spectra were collected using a FT-801 IR spectrometer (Simex, Russia) equipped with a Micran-3 microscope in ATR mode (Ge-ATR objective) and in trans-reflection mode (15x objective) for thin film cuts deposited onto a stainless steel plate with an optical resolution of 2 cm^{-1} in the range

 doi:10.20944/preprints202411.1343.v1

of 600-4000 cm^{-1} and an aperture of 100 μm. The ATR correction was implemented with standard parameter for the Ge-crystal.

TM4000II Tabletop scanning electron microscope (SEM) (Hitachi Ltd., Japan) with QUANTAX 75 (Bruker, USA) energy-dispersive (EDS) detector was used to visualize the morphology of the samples, check their chemical composition and thus prove the presence of the filler in the matrix, as well as to check the homogeneity of its distribution.

AFM was used to investigate the morphology and to study the mechanical properties of polymer-based nanocomposite samples. For this purpose, NTEGRA SPM (EMTION, Russia) was used first in the dynamic force (morphology scans) and then in the nanoindentation mode (force curve spectroscopy with mechanical response mapping). For this study we used NSG10 AFM tips with 3 nm curvature radius and a standard software from EMTION, Russia.

2.7. Magnetic Characterization

Magnetic properties of the nanocomposites were studied using Lake Shore 7400 series (Cryotronics Inc., USA) vibrating sample magnetometer (VSM) at room temperature ($\sim$297 K) with an external field varying in the range of $\pm$0.9 T. The polymer films were fixed to the quartz sample holder using a tape container. The approximation of hysteresis curves was used to calculate the main magnetic parameters: saturation magnetization (M_S), reduced residual magnetization (M_R/M_S), and coercivity field ($\mu_0 H_C$).

2.8. Photocatalysis and Piezocatalysis Study

The piezocatalytic and photocatalytic dye decomposition tests were carried out using UV-visible irradiation spectroscopy. A 250 W high pressure mercury lamp (Philips, Netherlands) was used as a source of UV-visible light. The distance from the light source to the reactor was 10 cm. Piezophotocatalytic decomposition was carried out in an ultrasonic bath with a power of 250 W at a frequency of 18 kHz. To eliminate the effect of temperature on the decomposition efficiency, the reactor was kept at a constant temperature of 26 °C. Before testing, a film (3$\times$1 cm^2, thickness – 25 μm, weight – 0.7 mg) was immersed in a beaker with a solution of methylene blue (MB) (1 mg L^{-1} , 20 mL) and kept in a dark place for 1 h to establish the adsorption–desorption balance. During the test, 3 ml of the sample solution was extracted every 15 min and analyzed using a UV-visible spectrometer. The dye concentration was measured from the maximum absorption peak of MB at λ = 663 nm. The described experiment was performed using a SF-200 spectrophotometer (OKB Spektr, Russia). The percentage of MB degradation was indicated as C/C_0 (C and C_0 are the measured and initial concentrations of MB in the dye solution, respectively).

3. Results and Discussion

3.1. Structural Characterization of Single Materials and Heterostructures

XRD analysis was performed to confirm the functionalization of MXenes with MNPs and additional delamination of MXenes under their growth as it was addressed in [37]. The results given in Figures 1a and 1b evidence the appearance of characteristic peaks from both MXenes and spinel ferrites (IO or CFO) in the XRD patterns of the obtained heterostructures. The pronounced increase in (002) MXene reflection at low angles, alongside with almost the complete vanishing of MAX phase reflections, suggests further delamination of MXenes mediated by MNPs growth, as was expected [37]. The size of iron oxide MNPs grown on $Ti_3C_2T_x$ MXene surface is larger than those for free-grown particles, in agreement with our previous findings [37], while the size of CFO particles practically does not change, which is due to the lower mass content of MXene in the respective heterostructure. The PEG coating does not alter the crystal structure of nanoparticles and heterostructures, nor does it introduce additional reflexes in the XRD patterns. The lattice parameters of the particles practically do not change with respect to the growth method (with or without MXenes): for iron oxide MNPs, it ranges between 0.834 nm for maghemite (γ-Fe_2O_3) and 0.839 nm for bulk magnetite (Fe_3O_4), aligning

 doi:10.20944/preprints202411.1343.v1

more closely with γ-Fe_2O_3. For CFO, the lattice constant is approximately 0.839 nm, similar to bulk cobalt ferrite. The respective parameters are summarized in Table 2.

Table 2. Size of crystallites (D_{XRD}) and lattice constants (a) of free-grown and MXene-heterostructured IO and CFO MNPs.

Sample	D_{XRD}, nm	a, Å
Fe_3O_4	10±1	8.352±0.007
$Ti_3C_2T_x/Fe_3O_4$	15±3	8.357±0.007
$CoFe_2O_4$	10±2	8.380±0.006
$Ti_3C_2T_x/CoFe_2O_4$	9±1	8.387±0.008

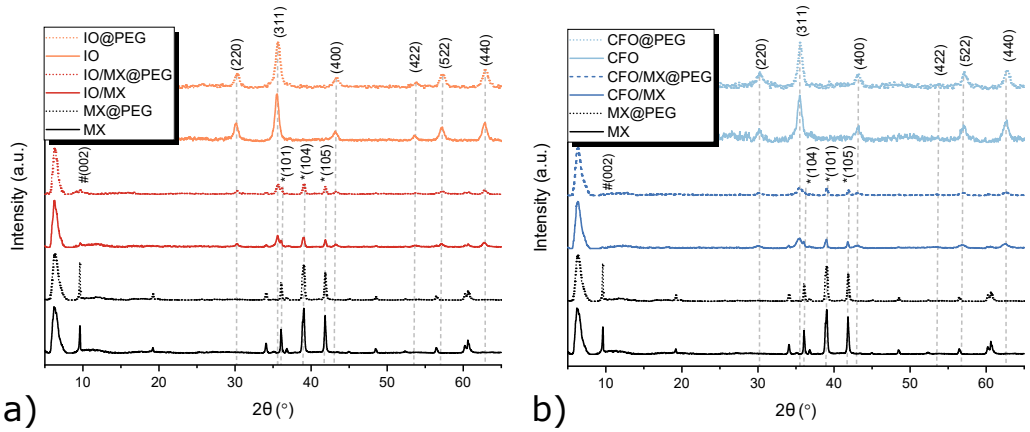

Figure 1. XRD patterns of: (a) $Ti_3C_2T_x$ MXenes, iron oxide, and (b) cobalt ferrite nanoparticles, and their respective heterostructures with and without PEG coating. Miller indices (hkl) are provided for major crystallographic planes of MXene (#), MAX phase (∗), and spinel structure.

Different polymorphs of PVDF can be distinguished by IR spectra [61], namely by the position of the bands of the νC-F stretchings (1000-1300 cm^{-1}) and the CH deformations (750-900 cm^{-1}). The β-phase is characterized by the νC-F bands at 1279 cm^{-1} and 1172 cm^{-1}, and the γ-phase – at 1234 and 1176 cm^{-1}, while the δCH bands at 880 and 841 cm^{-1} are indistinguishable. The α-phase is characterized by νC-F bands of 1214 and 1183 cm^{-1}, with δCH bands at 872, 795, and 764 cm^{-1}. Previous studies [62] indicate that the α-phase can be most easily identified by its δCH bands.

The obtained spectra of PVDF and its composites with different types of fillers are presented in Figure 2. Rather clearly, all the ATR FTIR spectra coincide with each other, while the transmission spectra differ only slightly in the intensity of the line at 1235 cm^{-1}. The bands located at 835, 876, 1071, 1169, 1231, and 1402 cm^{-1} are observed in all the ATR FTIR spectra, their shape, intensity distribution and position correspond to the predominance of the γ-phase on the surface, together with an amorphous phase and a very small amount of β-phase, the latter is observed as a weak band at 1275 cm^{-1}. The IR transmission spectra corresponding to the sample volume, show a strong band at 1274 cm^{-1} corresponding to the β-phase, and a weak band at 1231 cm^{-1}, which for some samples vanishes out due to more disordered phase. No α-phase bands were detected in the all spectra. In the IR spectra of the sample filled with PEG-coated nanoparticles, the IR lines referring to PEG cannot be detected due to its minor content. Thus, in all the examined samples PVDF possesses a phase composition consisting of the β-phase prevailing in the bulk of the film, γ-phase prevailing on the surface, as well as a significant amount of the disordered phase.

The evaluation of the phase composition of PVDF-based nanocomposite samples, revealed from the IR spectra, demonstrates very small content of paraelectric α-phase, which should be favorable for piezoelectric device applications. The predominance of the β-phase in the bulk of the material and the presence of the γ-phase on the surface indicate that the material is generally suitable for

 doi:10.20944/preprints202411.1343.v1

catalytic applications [63,64]. However, the presence of a significant amount of disordered phase may reduce the effectiveness of piezoelectric performance, since disordered structure rarely promotes the high level of crystallinity required to optimize piezoelectric properties. Thus, the phase composition, although advantageous, requires further investigation and optimization to achieve the best results for the claimed application.

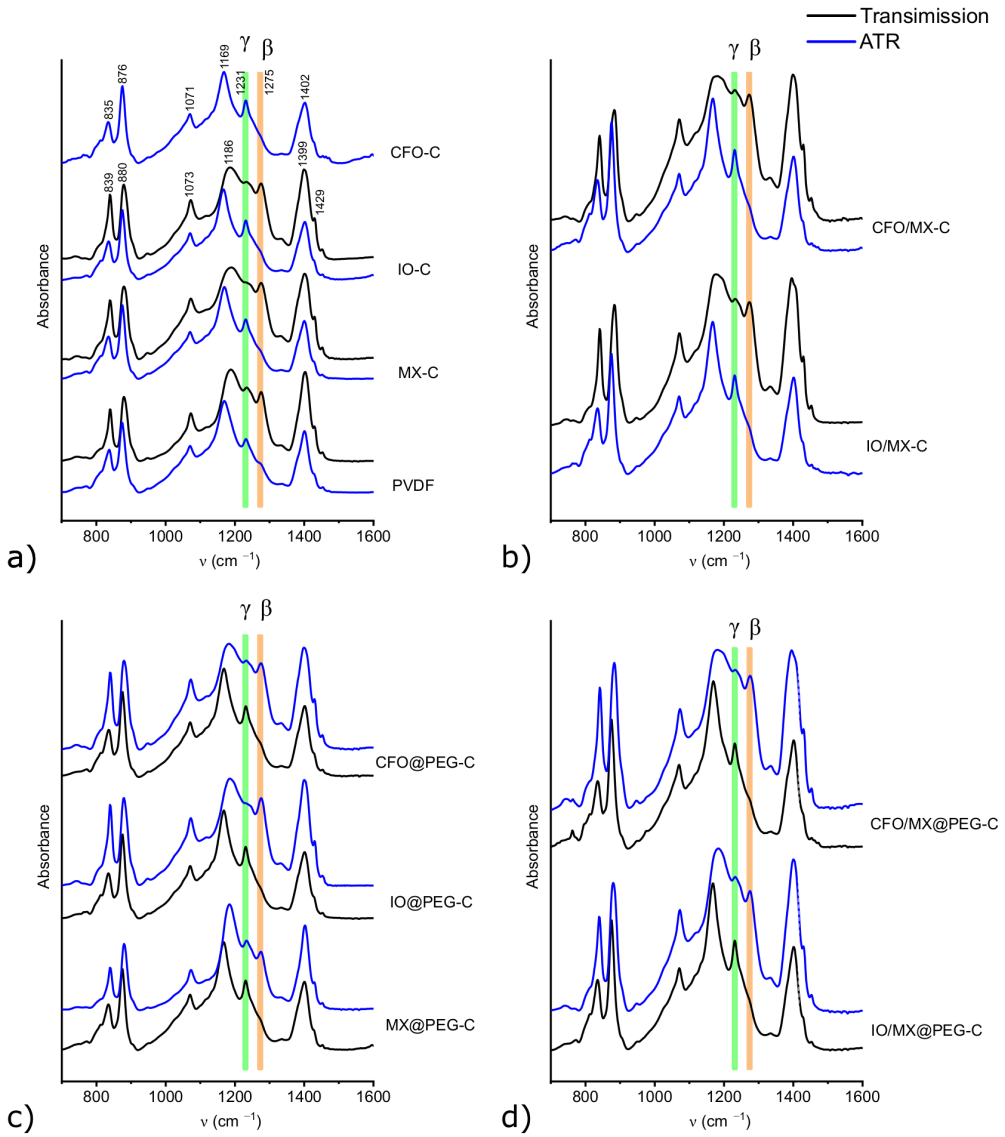

Figure 2. IR transmission (black) and ATR (blue) spectra of PVDF-based composites: (a) pure PVDF and single-filler composites, (b) MXene/magnetic heterostructure composites, (c) PEG-coated single-filler composites, and (d) PEG-coated heterostructure composites. Characteristic bands of γ- and β-phases are highlighted in green and orange, respectively.

Brief SEM examination let us confirm that PEG coating is advantageous for promoting better homogeneity of the filler particle distribution inside PVDF host matrix. Studies have shown that the incorporation of a polymer such as PEG into photocatalysis is very useful in enhancing the catalytic activity of the immobilized sample. PEG is a polymeric material that can be used to enhance the functionalization of a surface that acted as a matrix agent or as a structural control agent [65,66]. From the measurement of Young's modulus of the samples, it was obtained that its value increases when pure

 doi:10.20944/preprints202411.1343.v1

MXenes are added to the polymer, which is due to the reinforcing properties of MXenes [67]. When the filler nanoparticles are coated with PEG, the Young's modulus decreases compared to conventional nanoparticles, while for all the MXene-based fillers (single MXenes and heterostructures) PEG coating provides Young's modulus enhancement, which can also be explained by the better dispersibility.

3.2. Magnetic Properties of PVDF-Based Nanocomposites

Magnetization of PVDF-based nanocomposite samples versus the applied field was measured using VSM (see Figure 3). For composites with IO, the saturation magnetization of ~7.4 A m^2 kg^{-1} is roughly 10% of that of bulk γ-Fe_2O_3, which exhibits the M_S value of 73 A·m^2/kg at 300 K. This reduction is consistent with the weight fraction of MNPs in a non-magnetic matrix. Composites with MXene/IO heterostructures demonstrate a lower M_S value of ~4.4 A m^2 kg^{-1}. The presence of MXene significantly increases both the M_R/M_S ratio and $\mu_0 H_C$, with values rising from 0.02 to 0.10 and from ~2.4 mT to ~15 mT, respectively. This increase can be attributed to the larger size of IO nanoparticles in the MXene-containing samples, in agreement with the higher crystal size estimated from XRD. After coating the filler with PEG, the saturation magnetization further decreases to ~6.4 A m^2 kg^{-1} and ~3.6 A m^2 kg^{-1} for IO@PEG-C and IO/MX@PEG-C samples, respectively.

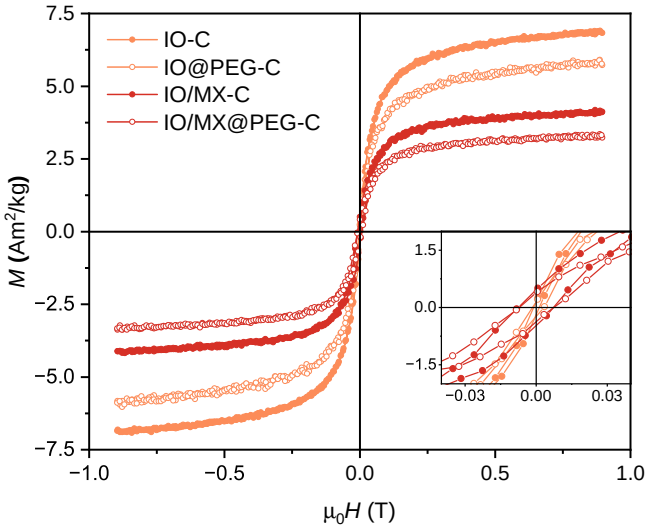

Figure 3. Magnetization versus applied field at 297 K for PVDF-based nanocomposites with Fe_3O_4 and MXene/Fe_3O_4 fillers (with and without PEG).

For the series of $CoFe_2O_4$-containing nanocomposites, the respective magnetic characterization results are provided in Figure 4. The saturation magnetization decreases from ~5.2 A m^2 kg^{-1} to ~3.2 A m^2 kg^{-1}, and from ~4.8 A m^2 kg^{-1} to ~2.9 A m^2 kg^{-1} for the PEG-coated CFO-C and CFO/MX-C samples, respectively. Here, there is almost no change in the value of saturation magnetization for CFO nanoparticles in these two types of samples: 5.2±0.5 A m^2 kg^{-1} and 4.3±0.4 A m^2 kg^{-1}, which is probably due to the approximately equal size of CFO particles obtained by simple co-precipitation (10±2) nm and grown on the surface of $Ti_3C_2T_x$ MXenes (9±1 nm). The magnetization of composites is smaller by a factor of 10 relative to solely particles and heterostructures, which is consistent with the mass component of the filler in the host matrix. Main magnetic parameters (M_S, M_R/M_S, $\mu_0 H_C$) of PVDF-based nanocomposites with different fillers are presented in Table 3.

The provided magnetic characterization lets us claim that our PVDF-based nanocomposite samples can be easily extracted from purified water under the application of an external magnetic field. IO-containing samples are a bit more promising in this case as they demonstrate more soft magnetic behavior with almost vanishing remanent magnetization.

 doi:10.20944/preprints202411.1343.v1

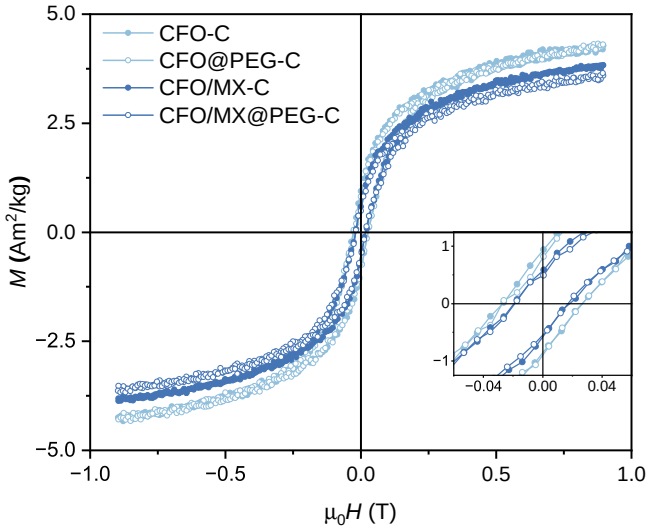

Figure 4. Magnetization versus applied field at 297 K for PVDF-based nanocomposites with CFO and MXene/CFO fillers (with and without PEG).

Table 3. Main magnetic parameters of magnetic particles and PVDF-based nanocomposites derived from the provided hysteresis measurements: the saturation magnetization (M_S), reduced remanent magnetization (M_R/M_S), coercive field ($\mu_0 H_C$).

Sample	M_S [A m^2 kg^{-1}]	M_R/M_S	$\mu_0 H_C$ [mT]
IO-C	7.4±0.7	0.02	2.4±0.1
IO@PEG-C	6.4±0.6	0.03	4.9±0.1
IO/MX-C	4.4±0.4	0.10	14.9±0.1
IO/MX@PEG-C	3.6±0.4	0.11	14.6±0.1
CFO-C	5.2±0.5	0.18	53.7±0.1
CFO@PEG-C	4.8±0.5	0.16	54.4±0.1
CFO/MX-C	4.3±0.4	0.13	37.7±0.1
CFO/MX@PEG-C	4.1±0.4	0.12	35.9±0.1

3.3. Photocatalysis and Piezocatalysis

Investigation of MB photocatalytic degradation under UV-visible light is presented in Figure 5, the results demonstrate the relative photocatalytic activity of different PVDF-based nanocomposite samples in the degradation process. The most efficient catalyst is the sample IO/MX@PEG-C, which provides a 45.8% degradation rate after 60 min. At the same time, CFO/MX@PEG-C, IO/MX-C and MX@PEG-C samples demonstrate less pronounced but still sufficiently high photocatalytic properties, with achieved degradation rates of 40.3%, 34.2% and 32.7%, respectively. The pure polymer material does not exhibit photocatalytic characteristics and shows only 9% degradation rate, which is probably due to its high light scattering coefficient [68].

The IO/MX@PEG-C composite exhibits excellent performance for photocatalysis due to the synergistic interaction between its components. $Ti_3C_2T_x$ MXene exhibits high conductivity and efficient charge separation, which enhances the photocatalytic activity of the composite. Combined with Fe_3O_4 magnetic nanoparticles, which possess intriguing photocatalytic properties along with soft ferromagnetism, the composite allows the photocatalyst to be easily separated from the solution after reaction, which facilitates its reuse.

PEG, on the other hand, improves the homogeneity of the filler distribution inside the polymer matrix, making the design of the composite more favorable. Thus, these factors make IO/MX@PEG-C

 doi:10.20944/preprints202411.1343.v1

an efficient photocatalyst capable of rapidly and efficiently degrading organic pollutants under light, which is particularly relevant for wastewater treatment applications.

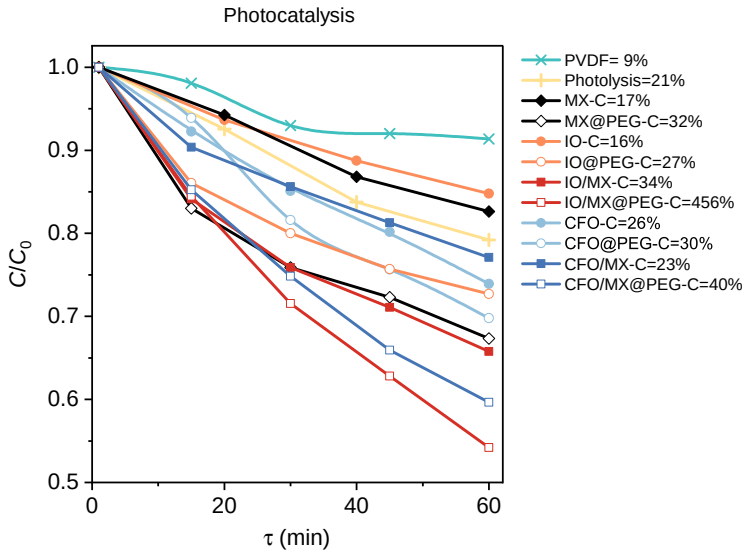

Figure 5. Time dependence of the photocatalytic dye removal from water mediated by various PVDF-based nanocomposite materials.

As shown in Figure 6, the sonocatalytic degradation effect of the CFO/MX@PEG-C sample reaches 45% after 60 min, not much exceeding the sonolysis efficiency of the control sample (pure PVDF) - 43%. When a sample is deformed by an external force from ultrasonic treatment, a polarization phenomenon occurs inside it, which generates positive and negative charges present on two relative surfaces. Thus, an effective conversion of the external force into electrical energy occurs and a polarization electric field is generated, which contributes to the occurrence of redox chemical reactions, leading to the generation of highly active oxygen species, which oxidize the MB [69–72].

In case of PVDF, the addition of fillers usually degrades its properties due to their agglomeration or insufficient dispersion in the polymer matrix. This can lead to a decrease in the polarization efficiency and a decrease in the overall performance of the material [64]. The utilization of CFO/MX@PEG-C in sonocatalysis is determined by several key factors that render this material particularly suitable for this field. First of all, $Ti_3C_2T_x$ MXene possesses a unique structure, characterized by a non-centrosymmetric lattice, allowing for the breaking of inversion symmetry and the induction of piezoelectric polarization. The presence of functional groups on the surface of MXenes, such as -O, -OH, and -F, further contributes to this effect, leading to pronounced piezoelectric behavior. The orientation and alignment of MXene layers within a composite matrix also play a crucial role in optimizing the piezoelectric response. These characteristics enhance its catalytic activity, making it an effective catalyst. When combined with $CoFe_2O_4$, which is also a powerful catalyst for various reactions, this hybrid material exhibits significantly improved catalytic performance in sonocatalytic processes. Furthermore, the combination of $Ti_3C_2T_x$ and $CoFe_2O_4$ creates a synergistic effect that enhances catalytic activity. $Ti_3C_2T_x$ facilitates the transfer of electrons and ions, while $CoFe_2O_4$ provides active sites for reactions. This interaction allows for achieving higher efficiency in sonocatalytic processes. Equally important is the aspect of stability. CFO/MX@PEG-C demonstrates good resistance to degradation under ultrasonic treatment and other conditions, making it a durable catalyst. The incorporation of PEG into the composition also contributes to improved stability of the catalyst.

 doi:10.20944/preprints202411.1343.v1

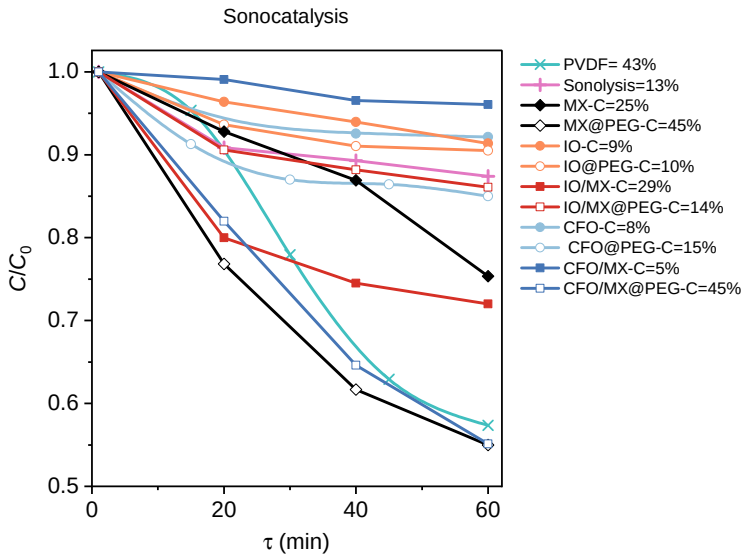

Figure 6. Time dependence of the sonocatalytic dye removal from water mediated by various PVDF-based nanocomposite materials.

4. Conclusions

In this work, $Ti_3C_2T_x$ MXenes were successfully functionalized with magnetic iron oxide (Fe_3O_4) and cobalt ferrite ($CoFe_2O_4$) nanoparticles, and then all of them (separately or in combination) were coated with PEG. The obtained flakes, particles and heterostructures were then added as fillers to PVDF polymer. The functionalization of MXenes with MNPs was confirmed by XRD, and additional delamination of multilayered MXenes was observed due to the growth of MNPs during a co-precipitation process. Notably, it was demonstrated that the addressed method of functionalization and delamination is applicable for the growth of particles of different compositions. FTIR results confirmed the presence of electroactive β-phase inside the PVDF polymer matrix and γ-phase on its surface, as well as a significant amount of the disordered phase. The presence of β and γ phases is desired for the proposed catalytic application, but further research is required to reduce the disordered phase.

The combination of properties of $Ti_3C_2T_x$, Fe_3O_4, and PEG in the IO/$Ti_3C_2T_x$@PEG-C composite makes it an effective and versatile piezo-photocatalyst that facilitates the rapid and efficient degradation of organic pollutants under the influence of ultrasound and light. Experimental studies have demonstrated that this composite achieves significant MB degradation rate, showing a reduction in MB concentration of over 45.8% within the treatment time of 60 minutes, confirming its high efficiency and potential for application in wastewater treatment. These findings highlight the promise of IO/$Ti_3C_2T_x$@PEG-C as one of the best candidates for photocatalytic processes. The CFO/$Ti_3C_2T_x$@PEG-C composite demonstrates remarkable potential for sonocatalysis, showcasing its ability to effectively degrade organic pollutants under ultrasonic irradiation. Experimental results indicate that this composite achieves a significant reduction in MB concentration, exceeding 45% within a treatment duration, which underscores its high efficiency and applicability in wastewater treatment. These findings highlight the promising nature of CFO/$Ti_3C_2T_x$@PEG-C as one of the leading candidates for sonocatalytic process, making it a valuable material for environmental remediation applications.

Author Contributions: Author Contributions: Conceptualization, N.S., K.S. and S.A.; methodology, A.O., K.S. and K.M.; formal analysis, A.O., K.S. and S.A.; investigation, N.S., S.A., V.R and R.A.; data curation, N.S., S.A. and K.S.; writing—original draft preparation, N.S., S.A. and K.S.; writing—review and editing, K.S. and A.O.; visualization, N.S., K.S., R.A. and S.A.; supervision, V.R.; project administration, K.M.; funding acquisition, K.M. and V.R. All authors have read and agreed to the published version of the manuscript.

 doi:10.20944/preprints202411.1343.v1

Funding: This work was carried out with financial support from the Russian Science Foundation (grant no. 22-12-20036), regional part no. 07-C/2022 https://rscf.ru/. The IR spectra were registered using the equipment of the Center for Molecular Composition Studies of INEOS RAS with financial support from the Ministry of Science and Higher Education of the Russian Federation (agreement no. 075-00277-24-00) https://minobrnauki.gov.ru/.

Conflicts of Interest: The authors declare no conflict of interest.

References

1. Mondal, S.; Purkait, M.K.; De, S. *Advances in Dye Removal Technologies*, 1 ed.; Green Chemistry and Sustainable Technology (GCST), Springer Singapore: Singapore, 2018; p. 323. 341 b/w illustrations, 21 illustrations in colour, doi:10.1007/978-981-10-6293-3.
2. Castillo-Suárez, L.A.; Sierra-Sánchez, A.G.; Linares-Hernández, I.; Martínez-Miranda, V.; Teutli-Sequeira, E.A. A critical review of textile industry wastewater: green technologies for the removal of indigo dyes. *International Journal of Environmental Science and Technology* **2023**, *20*, 10553–10590. doi:10.1007/s13762-023-04810-2.
3. Islam, T.; Repon, M.R.; Islam, T.; Sarwar, Z.; Rahman, M.M. Impact of textile dyes on health and ecosystem: a review of structure, causes, and potential solutions. *Environmental Science and Pollution Research* **2023**, *30*, 9207–9242. doi:10.1007/s11356-022-24398-3.
4. Jahan, N.; Tahmid, M.; Shoronika, A.Z.; Fariha, A.; Roy, H.; Pervez, M.N.; Cai, Y.; Naddeo, V.; Islam, M.S. A Comprehensive Review on the Sustainable Treatment of Textile Wastewater: Zero Liquid Discharge and Resource Recovery Perspectives. *Sustainability* **2022**, *14*. doi:10.3390/su142215398.
5. Yaseen, D.A.; Scholz, M. Textile dye wastewater characteristics and constituents of synthetic effluents: a critical review. *International Journal of Environmental Science and Technology* **2019**, *16*, 1193–1226. doi:10.1007/s13762-018-2130-z.
6. Azanaw, A.; Birlie, B.; Teshome, B.; Jemberie, M. Textile effluent treatment methods and eco-friendly resolution of textile wastewater. *Case Studies in Chemical and Environmental Engineering* **2022**, *6*, 100230. doi:10.1016/j.cscee.2022.100230.
7. Palani, G.; Arputhalatha, A.; Kannan, K.; Lakkaboyana, S.K.; Hanafiah, M.M.; Kumar, V.; Marella, R.K. Current Trends in the Application of Nanomaterials for the Removal of Pollutants from Industrial Wastewater Treatment—A Review. *Molecules* **2021**, *26*. doi:10.3390/molecules26092799.
8. Gadow, S.I.; Estrada, A.L.; Li, Y.Y. Characterization and potential of two different anaerobic mixed microflora for bioenergy recovery and decolorization of textile wastewater: Effect of C/N ratio, dye concentration and pH. *Bioresource Technology Reports* **2022**, *17*, 100886. doi:10.1016/j.biteb.2021.100886.
9. de Araújo, C.M.B.; Oliveira do Nascimento, G.F.; Bezerra da Costa, G.R.; Baptisttella, A.M.S.; Fraga, T.J.M.; de Assis Filho, R.B.; Ghislandi, M.G.; da Motta Sobrinho, M.A. Real textile wastewater treatment using nano graphene-based materials: Optimum pH, dosage, and kinetics for colour and turbidity removal. *The Canadian Journal of Chemical Engineering* **2020**, *98*, 1429–1440, [https://onlinelibrary.wiley.com/doi/pdf/10.1002/cjce.23712]. doi:10.1002/cjce.23712.
10. Nuengmatcha, P.; Kuyyogsuy, A.; Porrawatkul, P.; Pimsen, R.; Chanthai, S.; Nuengmatcha, P. Efficient degradation of dye pollutants in wastewater via photocatalysis using a magnetic zinc oxide/graphene/iron oxide-based catalyst. *Water Science and Engineering* **2023**, *16*, 243–251. doi:10.1016/j.wse.2023.01.004.
11. Khan, S.; Noor, T.; Iqbal, N.; Yaqoob, L. Photocatalytic Dye Degradation from Textile Wastewater: A Review. *ACS Omega* **2024**, *9*, 21751–21767. doi:10.1021/acsomega.4c00887.
12. Gupta, A.K.; Pal, A.; Sahoo, C. Photocatalytic degradation of a mixture of Crystal Violet (Basic Violet 3) and Methyl Red dye in aqueous suspensions using Ag^{+} doped TiO_2. *Dyes and Pigments* **2006**, *69*, 224–232. doi:10.1016/j.dyepig.2005.04.001.
13. McCullagh, C.; Skillen, N.; Adams, M.; Robertson, P.K. Photocatalytic reactors for environmental remediation: a review. *Journal of Chemical Technology & Biotechnology* **2011**, *86*, 1002–1017. doi:10.1002/jctb.2650.
14. Venkatachalam, N.; Palanichamy, M.; Murugesan, V. Sol–gel preparation and characterization of alkaline earth metal doped nano TiO_2: Efficient photocatalytic degradation of 4-chlorophenol. *Journal of Molecular Catalysis A: Chemical* **2007**, *273*, 177–185. doi:10.1016/j.molcata.2007.03.077.
15. Hong, K.S.; Xu, H.; Konishi, H.; Li, X. Direct Water Splitting Through Vibrating Piezoelectric Microfibers in Water. *The Journal of Physical Chemistry Letters* **2010**, *1*, 997–1002. doi:10.1021/jz100027t.

16. Hong, K.S.; Xu, H.; Konishi, H.; Li, X. Piezoelectrochemical Effect: A New Mechanism for Azo Dye Decolorization in Aqueous Solution through Vibrating Piezoelectric Microfibers. *The Journal of Physical Chemistry C* **2012**, *116*, 13045–13051, [https://doi.org/10.1021/jp211455z]. doi:10.1021/jp211455z.
17. Lin, H.; Wu, Z.; Jia, Y.; Li, W.; Zheng, R.K.; Luo, H. Piezoelectrically induced mechano-catalytic effect for degradation of dye wastewater through vibrating $Pb(Zr_{0.52}Ti_{0.48})O3$ fibers. *Applied Physics Letters* **2014**, *104*, 162907. doi:10.1063/1.4873522.
18. Zhang, Y.; Xie, M.; Adamaki, V.; Khanbareh, H.; Bowen, C.R. Control of electro-chemical processes using energy harvesting materials and devices. *Chem. Soc. Rev.* **2017**, *46*, 7757–7786. doi:10.1039/C7CS00387K.
19. Li, H.; Sang, Y.; Chang, S.; Huang, X.; Zhang, Y.; Yang, R.; Jiang, H.; Liu, H.; Wang, Z.L. Enhanced Ferroelectric-Nanocrystal-Based Hybrid Photocatalysis by Ultrasonic-Wave-Generated Piezophototronic Effect. *Nano Letters* **2015**, *15*, 2372–2379, [https://doi.org/10.1021/nl504630j]. PMID: 25803813, doi:10.1021/nl504630j.
20. Tan, C.F.; Ong, W.L.; Ho, G.W. Self-Biased Hybrid Piezoelectric-Photoelectrochemical Cell with Photocatalytic Functionalities. *ACS Nano* **2015**, *9*, 7661–7670, [https://doi.org/10.1021/acsnano.5b03075]. PMID: 26122026, doi:10.1021/acsnano.5b03075.
21. Liang, Z.; Yan, C.F.; Rtimi, S.; Bandara, J. Piezoelectric materials for catalytic/photocatalytic removal of pollutants: Recent advances and outlook. *Applied Catalysis B: Environmental* **2019**, *241*, 256–269. doi:10.1016/j.apcatb.2018.09.028.
22. Lin, H.M.; Chang, K.S. Synergistic piezophotocatalytic and photoelectrochemical performance of poly(vinylidene fluoride)–$ZnSnO_3$ and poly(methyl methacrylate)–$ZnSnO_3$ nanocomposites. *RSC Adv.* **2017**, *7*, 30513–30520. doi:10.1039/C7RA05175A.
23. He, H.; Fu, Y.; Zang, W.; Wang, Q.; Xing, L.; Zhang, Y.; Xue, X. A flexible self-powered T-ZnO/PVDF/fabric electronic-skin with multi-functions of tactile-perception, atmosphere-detection and self-clean. *Nano Energy* **2017**, *31*, 37–48. doi:10.1016/j.nanoen.2016.11.020.
24. Jamal, M.A.; Ahmad Sajid, T.; Saeed, M.; Naseem, B.; Muneer, M. Explication of molecular interactions between leucine and pharmaceutical active ionic liquid in an aqueous system: Volumetric and acoustic studies. *Journal of Molecular Liquids* **2022**, *360*, 119510. doi:10.1016/j.molliq.2022.119510.
25. Ghows, N.; Entezari, M.H. Exceptional catalytic efficiency in mineralization of the reactive textile azo dye (RB5) by a combination of ultrasound and core–shell nanoparticles (CdS/TiO_2). *Journal of Hazardous Materials* **2011**, *195*, 132–138. doi:10.1016/j.jhazmat.2011.08.049.
26. Khataee, A.; Karimi, A.; Arefi-Oskoui, S.; Darvishi Cheshmeh Soltani, R.; Hanifehpour, Y.; Soltani, B.; Joo, S.W. Sonochemical synthesis of Pr-doped ZnO nanoparticles for sonocatalytic degradation of Acid Red 17. *Ultrasonics Sonochemistry* **2015**, *22*, 371–381. doi:10.1016/j.ultsonch.2014.05.023.
27. Shirsath, S.; Pinjari, D.; Gogate, P.; Sonawane, S.; Pandit, A. Ultrasound assisted synthesis of doped TiO_2 nano-particles: Characterization and comparison of effectiveness for photocatalytic oxidation of dyestuff effluent. *Ultrasonics Sonochemistry* **2013**, *20*, 277–286. doi:10.1016/j.ultsonch.2012.05.015.
28. Hao, A.; Ning, X.; Cao, Y.; Xie, J.; Jia, D. Boosting the piezocatalytic performance of Bi_2WO_6 nanosheets towards the degradation of organic pollutants. *Mater. Chem. Front.* **2020**, *4*, 2096–2102. doi:10.1039/D0QM00179A.
29. Nie, Q.; Xie, Y.; Ma, J.; Wang, J.; Zhang, G. High piezo–catalytic activity of ZnO/Al_2O_3 nanosheets utilizing ultrasonic energy for wastewater treatment. *Journal of Cleaner Production* **2020**, *242*, 118532. doi:10.1016/j.jclepro.2019.118532.
30. Feng, W.; Yuan, J.; Zhang, L.; Hu, W.; Wu, Z.; Wang, X.; Huang, X.; Liu, P.; Zhang, S. Atomically thin ZnS nanosheets: Facile synthesis and superior piezocatalytic H_2 production from pure H_2O. *Applied Catalysis B: Environmental* **2020**, *277*, 119250. doi:10.1016/j.apcatb.2020.119250.
31. Tian, W.; Qiu, J.; Li, N.; Chen, D.; Xu, Q.; Li, H.; He, J.; Lu, J. Efficient piezocatalytic removal of BPA and Cr(VI) with SnS_2/CNFs membrane by harvesting vibration energy. *Nano Energy* **2021**, *86*, 106036. doi:10.1016/j.nanoen.2021.106036.
32. Bagchi, B.; Hoque, N.A.; Janowicz, N.; Das, S.; Tiwari, M.K. Re-usable self-poled piezoelectric/piezocatalytic films with exceptional energy harvesting and water remediation capability. *Nano Energy* **2020**, *78*, 105339. doi:10.1016/j.nanoen.2020.105339.
33. Ma, W.; Yao, B.; Zhang, W.; He, Y.; Yu, Y.; Niu, J. Fabrication of PVDF-based piezocatalytic active membrane with enhanced oxytetracycline degradation efficiency through embedding few-layer E-MoS_2 nanosheets. *Chemical Engineering Journal* **2021**, *415*, 129000. doi:10.1016/j.cej.2021.129000.

34. Rabadanova, A.; Abdurakhmanov, M.; Gulakhmedov, R.; Shuaibov, A.; Selimov, D.; Sobola, D.; Částková, K.; Ramazanov, S.; Orudzhev, F. Piezo-, photo- and piezophotocatalytic activity of electrospun fibrous PVDF/CTAB membrane. *Chimica Techno Acta* **2022**, *9*, 20229420. doi:10.15826/chimtech.2022.9.4.20.
35. Gogotsi, Y.; Huang, Q. MXenes: Two-Dimensional Building Blocks for Future Materials and Devices. *ACS Nano* **2021**, *15*, 5775–5780, [https://doi.org/10.1021/acsnano.1c03161]. doi:10.1021/acsnano.1c03161.
36. Patra, S.; Kiran, N.U.; Mane, P.; Chakraborty, B.; Besra, L.; Chatterjee, S.; Chatterjee, S. Hydrophobic MXene with enhanced electrical conductivity. *Surfaces and Interfaces* **2023**, *39*, 102969. doi:10.1016/j.surfin.2023.102969.
37. Sobolev, K.; Omelyanchik, A.; Shilov, N.; Gorshenkov, M.; Andreev, N.; Comite, A.; Slimani, S.; Peddis, D.; Ovchenkov, Y.; Vasiliev, A.; Magomedov, K.E.; Rodionova, V. Iron Oxide Nanoparticle-Assisted Delamination of $Ti_3C_2T_x$ MXenes: A New Approach to Produce Magnetic MXene-Based Composites. *Nanomaterials* **2024**, *14*. doi:10.3390/nano14010097.
38. Anasori, B.; Gogotsi, Y. MXenes: trends, growth, and future directions. *Graphene and 2D Materials* **2022**, *7*, 75–79. doi:10.1007/s41127-022-00053-z.
39. Sobolev, K.V.; Magomedov, K.E.; Shilov, N.R.; Rodionova, V.V.; Omelyanchik, A.S. Adsorption of Copper Ions on the Surface of Multilayer $Ti_3C_2T_x$ MXenes with Mixed Functionalization. *Nanobiotechnology Reports* **2023**, *18*, S84–S89. doi:10.1134/S2635167623600955.
40. Zhang, Y.; Wang, L.; Zhang, N.; Zhou, Z. Adsorptive environmental applications of MXene nanomaterials: a review. *RSC Adv.* **2018**, *8*, 19895–19905. doi:10.1039/C8RA03077D.
41. Ijaz, I.; Bukhari, A.; Gilani, E.; Nazir, A.; Zain, H.; Bukhari, A.; Shaheen, A.; Hussain, S.; Imtiaz, A. Functionalization of chitosan biopolymer using two dimensional metal-organic frameworks and MXene for rapid, efficient, and selective removal of lead (II) and methyl blue from wastewater. *Process Biochemistry* **2023**, *129*, 257–267. doi:10.1016/j.procbio.2023.03.029.
42. Kashif, S.; Akram, S.; Murtaza, M.; Amjad, A.; Shah, S.S.A.; Waseem, A. Development of MOF-MXene composite for the removal of dyes and antibiotic. *Diamond and Related Materials* **2023**, *136*, 110023. doi:10.1016/j.diamond.2023.110023.
43. Tabrizi Hafez Moghaddas, S.M.; Elahi, B.; Javanbakht, V. Biosynthesis of pure zinc oxide nanoparticles using Quince seed mucilage for photocatalytic dye degradation. *Journal of Alloys and Compounds* **2020**, *821*, 153519. doi:10.1016/j.jallcom.2019.153519.
44. Vaez, Z.; Javanbakht, V. Synthesis, characterization and photocatalytic activity of ZSM-5/ZnO nanocomposite modified by Ag nanoparticles for methyl orange degradation. *Journal of Photochemistry and Photobiology A: Chemistry* **2020**, *388*, 112064. doi:10.1016/j.jphotochem.2019.112064.
45. Mirzaei, S.; Javanbakht, V. Dye removal from aqueous solution by a novel dual cross-linked biocomposite obtained from mucilage of Plantago Psyllium and eggshell membrane. *International Journal of Biological Macromolecules* **2019**, *134*, 1187–1204. doi:10.1016/j.ijbiomac.2019.05.119.
46. Mehrabi, M.; Javanbakht, V. Photocatalytic degradation of cationic and anionic dyes by a novel nanophotocatalyst of $TiO_2/ZnTiO_3/\alpha Fe_2O_3$ by ultraviolet light irradiation. *Journal of Materials Science: Materials in Electronics* **2018**, *29*, 9908–9919. doi:10.1007/s10854-018-9033-0.
47. Erfani, M.; Javanbakht, V. Methylene Blue removal from aqueous solution by a biocomposite synthesized from sodium alginate and wastes of oil extraction from almond peanut. *International Journal of Biological Macromolecules* **2018**, *114*, 244–255. doi:10.1016/j.ijbiomac.2018.03.003.
48. Bayat, M.; Javanbakht, V.; Esmaili, J. Synthesis of zeolite/nickel ferrite/sodium alginate bionanocomposite via a co-precipitation technique for efficient removal of water-soluble methylene blue dye. *International Journal of Biological Macromolecules* **2018**, *116*, 607–619. doi:10.1016/j.ijbiomac.2018.05.012.
49. Aeenjan, F.; Javanbakht, V. Methylene blue removal from aqueous solution by magnetic clinoptilolite/chitosan/EDTA nanocomposite. *Research on Chemical Intermediates* **2018**, *44*, 1459–1483. doi:10.1007/s11164-017-3179-x.
50. Bauer, R.; Waldner, G.; Fallmann, H.; Hager, S.; Klare, M.; Krutzler, T.; Malato, S.; Maletzky, P. The photo-fenton reaction and the TiO_2/UV process for waste water treatment—novel developments. *Catalysis Today* **1999**, *53*, 131–144. doi:10.1016/S0920-5861(99)00108-X.
51. William H. Glaze, J.W.K.; Chapin, D.H. The Chemistry of Water Treatment Processes Involving Ozone, Hydrogen Peroxide and Ultraviolet Radiation. *Ozone: Science & Engineering* **1987**, *9*, 335–352, [https://doi.org/10.1080/01919518708552148]. doi:10.1080/01919518708552148.

52. Ítalo Lacerda Fernandes.; Pereira Barbosa, D.; Botelho de Oliveira, S.; Antônio da Silva, V.; Henrique Sousa, M.; Montero-Muñoz, M.; A. H. Coaquira, J. Synthesis and characterization of the MNP@SiO_2@TiO_2 nanocomposite showing strong photocatalytic activity against methylene blue dye. *Applied Surface Science* **2022**, *580*, 152195. doi:10.1016/j.apsusc.2021.152195.
53. Mahdikhah, V.; Saadatkia, S.; Sheibani, S.; Ataie, A. Outstanding photocatalytic activity of $CoFe_2O_4$ /rGO nanocomposite in degradation of organic dyes. *Optical Materials* **2020**, *108*, 110193. doi:10.1016/j.optmat.2020.110193.
54. Zheng, Z.; He, J.; Zhang, Z.; Kumar, A.; Khan, M.; Lung, C.W.; Lo, I.M.C. Magnetically recyclable nanophotocatalysts in photocatalysis-involving processes for organic pollutant removal from wastewater: current status and perspectives. *Environ. Sci.: Nano* **2024**, *11*, 1784–1816. doi:10.1039/D3EN00906H.
55. Berni, A.; Mennig, M.; Schmidt, H., Doctor Blade. In *Sol-Gel Technologies for Glass Producers and Users*; Aegerter, M.A.; Mennig, M., Eds.; Springer US: Boston, MA, 2004; pp. 89–92. doi:10.1007/978-0-387-88953-5_10.
56. de Oliveira Guidolin, T.; Possolli, N.M.; Polla, M.B.; Wermuth, T.B.; Franco de Oliveira, T.; Eller, S.; Klegues Montedo, O.R.; Arcaro, S.; Cechinel, M.A.P. Photocatalytic pathway on the degradation of methylene blue from aqueous solutions using magnetite nanoparticles. *Journal of Cleaner Production* **2021**, *318*, 128556. doi:10.1016/j.jclepro.2021.128556.
57. Peng, C.; Wang, C.A.; Song, Y.; Huang, Y. A novel simple method to stably synthesize Ti_3AlC_2 powder with high purity. *Materials Science and Engineering: A* **2006**, *428*, 54–58. doi:10.1016/j.msea.2006.04.042.
58. Lu, X.; Zhou, Y. Pressureless Sintering and Properties of Ti_3AlC_2. *International Journal of Applied Ceramic Technology* **2010**, *7*, 744–751, [https://ceramics.onlinelibrary.wiley.com/doi/pdf/10.1111/j.1744-7402.2009.02403.x]. doi:10.1111/j.1744-7402.2009.02403.x.
59. Ghidiu, M.; Lukatskaya, M.R.; Zhao, M.Q.; Gogotsi, Y.; Barsoum, M.W. Conductive two-dimensional titanium carbide 'clay'with high volumetric capacitance. *Nature* **2014**, *516*, 78–81. doi:10.1038/nature13970.
60. Omelyanchik, A.S.; Sobolev, K.V.; Shilov, N.R.; Andreev, N.V.; Gorshenkov, M.V.; Rodionova, V.V. Modification of the Codeposition Method for the Synthesis of Iron-Oxide Nanoparticles with a High Magnetization Value and a Controlled Reaction Yield. *Nanobiotechnology Reports* **2023**, *18*, 879–885. doi:10.1134/S2635167623600645.
61. Boccaccio, T.; Bottino, A.; Capannelli, G.; Piaggio, P. Characterization of PVDF membranes by vibrational spectroscopy. *Journal of Membrane Science* **2002**, *210*, 315–329. doi:10.1016/S0376-7388(02)00407-6.
62. Ramesh, D.; D'Souza, N.A. One-step fabrication of biomimetic PVDF-$BaTiO_3$ nanofibrous composite using DoE. *Materials Research Express* **2018**, *5*, 085308. doi:10.1088/2053-1591/aad156.
63. Abd El-Aziz, A.M.; Afifi, M. Influence the β-PVDF phase on structural and elastic properties of PVDF/PLZT composites. *Materials Science and Engineering: B* **2024**, *301*, 117152. doi:10.1016/j.mseb.2023.117152.
64. Auliya, R.Z.; Ooi, P.C.; Sadri, R.; Talik, N.A.; Yau, Z.Y.; Mohammad Haniff, M.A.S.; Goh, B.T.; Dee, C.F.; Aslfattahi, N.; Al-Bati, S.; Ibtehaj, K.; Hj Jumali, M.H.; Mohd Razip Wee, M.F.; Mohamed, M.A.; Othman, M. Exploration of 2D Ti_3C_2 MXene for all solution processed piezoelectric nanogenerator applications. *Scientific Reports* **2021**, *11*, 17432. doi:10.1038/s41598-021-96909-0.
65. Marija, M.; M., N.L. Modification of TiO_2 nanoparticles through lanthanum doping and peg templating. *Processing and Application of Ceramics* **2014**, *8*, 195–202. doi:10.2298/PAC1404195M.
66. Chang, H.; Jo, E.H.; Jang, H.D.; Kim, T.O. Synthesis of PEG-modified TiO_2–$InVO_4$ nanoparticles via combustion method and photocatalytic degradation of methylene blue. *Materials Letters* **2013**, *92*, 202–205. doi:10.1016/j.matlet.2012.11.006.
67. Zhao, Q.; Yang, L.; Ma, Y.; Huang, H.; He, H.; Ji, H.; Wang, Z.; Qiu, J. Highly sensitive, reliable and flexible pressure sensor based on piezoelectric PVDF hybrid film using MXene nanosheet reinforcement. *Journal of Alloys and Compounds* **2021**, *886*, 161069. doi:10.1016/j.jallcom.2021.161069.
68. Orudzhev, F.; Alikhanov, N.; Amirov, A.; Rabadanova, A.; Selimov, D.; Shuaibov, A.; Gulakhmedov, R.; Abdurakhmanov, M.; Magomedova, A.; Ramazanov, S.; Sobola, D.; Giraev, K.; Amirov, A.; Rabadanov, K.; Gadzhimagomedov, S.; Murtazali, R.; Rodionova, V. Porous Hybrid PVDF/$BiFeO_3$ Smart Composite with Magnetic, Piezophotocatalytic, and Light-Emission Properties. *Catalysts* **2023**, *13*. doi:10.3390/catal13050874.
69. Zhang, S.; Cai, M.; Wu, J.; Wang, Z.; Lu, X.; Li, K.; Lee, J.M.; Min, Y. photocatalytic degradation of TiO_2 via incorporating Ti_3C_2 MXene for methylene blue removal from water. *Catalysis Communications* **2023**, *174*, 106594. doi:https://doi.org/10.1016/j.catcom.2022.106594.

 doi:10.20944/preprints202411.1343.v1

70. Nasri, M.S.I.; Samsudin, M.F.R.; Tahir, A.A.; Sufian, S. Effect of MXene Loaded on g-C_3N_4 Photocatalyst for the Photocatalytic Degradation of Methylene Blue. *Energies* **2022**, *15*. doi:10.3390/en15030955.
71. My Tran, N.; Thanh Hoai Ta, Q.; Sreedhar, A.; Noh, J.S. $Ti_3C_2T_x$ MXene playing as a strong methylene blue adsorbent in wastewater. *Applied Surface Science* **2021**, *537*, 148006. doi:10.1016/j.apsusc.2020.148006.
72. Liu, T.; Li, L.; Geng, X.; Yang, C.; Zhang, X.; Lin, X.; Lv, P.; Mu, Y.; Huang, S. Heterostructured MXene-derived oxides as superior photocatalysts for MB degradation. *Journal of Alloys and Compounds* **2022**, *919*, 165629. doi:10.1016/j.jallcom.2022.165629.